



1 **Easy-to-use spatial Random Forest-based downscaling-calibration method for**
2 **producing high resolution and accurate precipitation data**

3 Chuanfa Chen^{1,2}, Baojian Hu^{1,2}, Yanyan Li^{1,2*}

4 ¹ College of Geodesy and Geomatics, Shandong University of Science and
5 Technology, Qingdao 266590, China

6 ² Key Laboratory of Geomatics and Digital Technology of Shandong Province,
7 Shandong University of Science and Technology, Qingdao 266590, China

8 * Correspondence: Yanyan Li (yylee@whu.edu.cn)

9 **Abstract**

10 High resolution and accurate precipitation data is significantly important for
11 numerous hydrological applications. To enhance the spatial resolution and accuracy of
12 satellite-based precipitation products, an easy-to-use downscaling-calibration method
13 based on spatial Random Forest (SRF) is proposed in this paper, where the spatial
14 autocorrelation between precipitation measurements is taken into account. The
15 proposed method consists of two main stages. Firstly, the satellite-based precipitation
16 was downscaled by SRF with the incorporation of some high-resolution covariates
17 including latitude, longitude, DEM, NDVI, terrain slope, aspect, relief, and land
18 surface temperatures. Then, the downscaled precipitation was calibrated by SRF with
19 rain gauge observations and the aforementioned high-resolution variables. The
20 monthly Integrated MultisatellitE Retrievals for Global Precipitation Measurement
21 (IMERG) located in Sichuan province, China from 2015 to 2019 was processed using
22 our method and its results were compared with those of some classical methods



23 including geographically weighted regression (GWR), artificial neural network
24 (ANN), random forest (RF), kriging interpolation only on gauge measurements,
25 bilinear interpolation-based downscaling and then SRF-based calibration (Bi-SRF),
26 and SRF-based downscaling and then geographical difference analysis (GDA)-based
27 calibration (SRF-GDA). Results show that: (1) the proposed method outperforms the
28 other methods as well as the original IMERG; (2) the monthly-based SRF estimation
29 is slightly more accurate than the annual-based SRF fraction disaggregation method;
30 (3) SRF-based downscaling and calibration preforms better than bilinear downscaling
31 (Bi-SRF) and GDA-based calibration (SRF-GDA); (4) kriging seems more accurate
32 than GWR and ANN in terms of quantitative accuracy measures, whereas its
33 precipitation map cannot capture the detailed spatial precipitation patterns; and (5)
34 among the predictors for calibration, the precipitation interpolated by kriging on the
35 gauge measurements is the most important variable, indicating the significance for the
36 inclusion of spatial autocorrelation information in gauge measurements.

37 **Keywords:** IMERG; Downscaling; Calibration; Machine learning; Interpolation

38 **1. Introduction**

39 Precipitation is an important variable for promoting our understanding of
40 hydrological cycle and water resource management (Chen et al., 2010). Previous
41 studies showed that about 70-80% of hydrological modeling errors were caused by
42 precipitation data uncertainties (Gebregiorgis and Hossain, 2013). However,
43 precipitation is also the most difficult meteorological factor to estimate due to its high



44 spatial and temporal heterogeneity (Beck et al., 2019). Although rain gauge
45 observations are reliable and accurate, it is difficult to reflect the spatial precipitation
46 pattern with the sparse and uneven distribution and limited coverage, especially in
47 remote and mountainous areas (Ullah et al., 2020).

48 During the past decades, plenty of satellite-based precipitation datasets have been
49 produced at regional, quasi-global and fully global scales, such as the Climate
50 Hazards Group Infrared Precipitation with Station data (CHIRPS, 0.05°) (Funk et al.,
51 2015), the Precipitation Estimation from Remotely Sensed Information using
52 Artificial Neural Networks-Climate Data Record (PERSIANN-CDR, 0.25°) (Ashouri
53 et al., 2015), the Climate Prediction Center (CPC) morphing technique (CMORPH,
54 0.25°) (Haile et al., 2013), the Multi-Source Weighted-Ensemble Precipitation
55 (MSWEP, 0.1°) (Beck et al., 2017), the Tropical Rainfall Measuring Mission (TRMM)
56 Multi-satellite Precipitation Analysis (TMPA, 0.25°) (Huffman et al., 2007) and the
57 Integrated MultisatellitE Retrievals for Global Precipitation Measurement (GPM)
58 mission (IMERG, 0.1°) (Hou et al., 2014). Nevertheless, these products are
59 characterized by considerable systematic biases due to the shortcomings of retrieval
60 algorithms, sensor capability and spatiotemporal collection frequency (Chen et al.,
61 2018; Wu et al., 2018; Yang et al., 2017). Moreover, their resolutions (from 0.05° to
62 2.5°) are too coarse to describe meso- and micro-scale precipitation patterns for
63 hydrological studies at local and basin scales (Immerzeel et al., 2009). Hence,
64 downscaling and calibration with the intention of improving the resolution and quality
65 of satellite-based precipitation datasets has become an essential step prior to various



66 hydrological applications at local scales (Bhuiyan et al., 2018).

67 Downscaling provides an effective way to derive high resolution precipitation
68 products, which is generally achieved by constructing the relationship between
69 precipitation and environmental variables at a coarse scale, and then putting the
70 high-resolution variables into the constructed model to downscale the precipitation
71 data from the coarse resolution to the fine (Chen et al., 2010; Immerzeel et al., 2009).
72 At present, many downscaling models have been proposed. For example, Immerzeel
73 et al. (2009) employed an exponential regression (ER) to describe the relationship
74 between Tropical Rainfall Measuring Mission (TRMM) and Normalized Difference
75 Vegetation Index (NDVI). Jia et al. (2011) used a multiple linear regression model
76 (MLR) to establish the relationship between TRMM, digital elevation model (DEM)
77 and NDVI. Duan and Bastiaanssen (2013) proposed a downscaling model based on
78 the second-order polynomial relationship between TRMM and NDVI. Considering
79 the heterogeneous relationship between precipitation and the land surface variables
80 across the study areas, geographically weighted regression (GWR) was commonly
81 adopted (Chen et al., 2015; Chen et al., 2014; Chen et al., 2020c; Li et al., 2019; Lu et
82 al., 2020; Xu et al., 2015), and showed more accurate results than ER and MLR. In
83 the recent decade, some data-driven machine learning (ML) methods such as random
84 forests (RF) (Shi et al., 2015; Zhang et al., 2021), support vector machine (SVM)
85 (Chen et al., 2010; Jing et al., 2016) and artificial neural network (ANN) (Elnashar et
86 al., 2020) were employed to capture the complex nonlinear relationship between
87 precipitation and the predictors. However, the downscaled precipitation products



88 inevitably contain large systematic biases.

89 To alleviate the inherent biases, many calibration methods have been proposed for
90 merging gauge observations and satellite-based precipitation to improve the accuracy
91 and spatial coverage of precipitation, such as nonparametric kernel smoothing method
92 (Li and Shao, 2010), geographical difference analysis (GDA) (Cheema and
93 Bastiaanssen, 2012), geographical ratio analysis (GRA) (Duan and Bastiaanssen,
94 2013), conditional merging (CM) (Berndt et al., 2014), quantile mapping (Chen et al.,
95 2013; Zhang and Tang, 2015), optimal interpolation (Lu et al., 2020; Wu et al., 2018;
96 Xie and Xiong, 2011), GWR (Chao et al., 2018; Chen et al., 2018; Lu et al., 2019) and
97 geostatistical interpolation (Park et al., 2017). However, these methods are based on
98 some strict assumptions which might not be satisfied in practice (Wu et al., 2020;
99 Zhang et al., 2021). Moreover, the precipitation-related environmental variables were
100 not taken into account. To this end, ML-based calibration methods have become
101 popular, such as Quantile Regression Forests (QRF) (Bhuiyan et al., 2018), ANN
102 (Pham et al., 2020; Yang and Luo, 2014), deep neural network (Tao et al., 2016), RF
103 (Baez-Villanueva et al., 2020), convolutional neural network (CNN) (Wu et al., 2020),
104 SVM and extreme learning machine (Zhang et al., 2021). In contrast, RF with
105 excellent results has been widely adopted in plenty of studies (Baez-Villanueva et al.,
106 2020; Bhuiyan et al., 2020).

107 In the context of downscaling and calibration of precipitation data, the merits of the
108 ML-based methods include (Hengl et al., 2018; Zhang et al., 2021): (i) they require no
109 strict statistical assumptions; (ii) they can capture complex nonlinear relationship



110 between precipitation and the environmental variables; (iii) they can include various
111 types of predictors, without suffering from the collinearity problem and (iv) they are
112 generally more accurate than the classical regression methods. However, there are at
113 least two limitations: (i) the ML algorithms were simply taken as a statistical tool
114 without considering the spatial autocorrelation between precipitation measurements;
115 and (ii) the ML algorithms were adopted in either downscaling or calibration, without
116 being used in both downscaling and calibration. More specifically, some (Jing et al.,
117 2016; Karbalaye Ghorbanpour et al., 2021; Yan et al., 2021) attempted to use the ML
118 methods for downscaling and then use the classical method (e.g. GDA and cokriging)
119 for calibration, while some (Zhang et al., 2021) employed the classical interpolation
120 methods (e.g. bilinear interpolation and kriging) for downscaling and then used the
121 ML methods for calibration. However, we regard that the use of ML methods in both
122 of downscaling and calibration could further improve the accuracy of precipitation,
123 since the high resolution environmental variables with valuable information can be
124 fully used in the two stages. To the best of our knowledge, no previous studies have
125 used the ML technique in both downscaling and calibration with the consideration of
126 high resolution environmental variables, simultaneously.

127 Based on aforementioned discussion, the objectives of this study are twofold: (i) to
128 develop an easy-to-use spatial RF (SRF) by taking into account the spatial
129 autocorrelation between adjacent gauge measurements, and (ii) to propose a
130 downscaling-calibration method based on SRF for producing high resolution and
131 accurate precipitation data. The use of RF as the basic model in our study is mainly



132 due to its high interpolation accuracy and low computational cost (Belgiu et al., 2016;
133 Mohsenzadeh Karimi et al., 2020).

134 Overall, the proposed method consists of two main steps. First, the precipitation
135 data is downscaled by SRF with the incorporation of some environmental variables
136 including DEM, NDVI, land surface temperatures (LSTs), terrain parameters, latitude
137 and longitude as recommended in previous studies (Jing et al., 2016; Li et al., 2019).
138 Second, SRF and the environmental variables were further used for merging the
139 downscaled precipitation data and gauge observations to boost the accuracy of the
140 precipitation data. The merit of the proposed method is that a new spatial RF is
141 developed for both downscaling and calibration of precipitation products, with the
142 incorporation of high-resolution environmental variables.

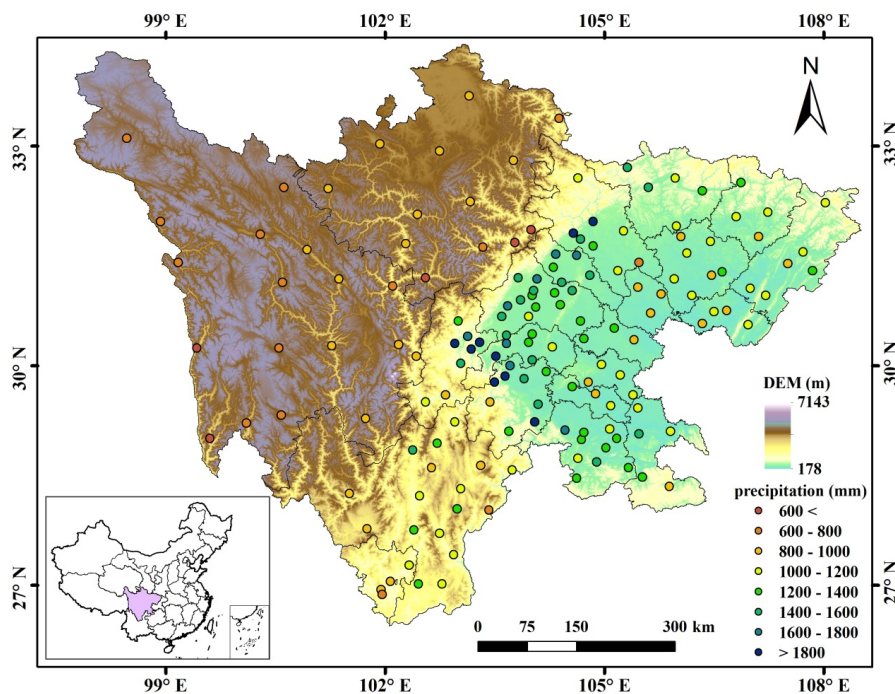
143 **2 Study area and dataset**

144 ***2.1. Study area***

145 Sichuan province between 97°21'-108°31'E and 26°03'-34°19'N was selected as the
146 study area (Fig. 1). It is situated between the Qinghai-Tibet Plateau and the Plain of
147 the Middle-and-lower Reaches of Yangtze River, with an area of 486,000 km².
148 Sichuan province has a complex and varied topography consisting of mountains, hills,
149 plain basins and plateaus with the elevation ranging from approximately 180 m in the
150 east to 7100 m in the west. Due to the different topographies in the west and east, the
151 climate has a significant difference. The east basin has subtropical monsoon climate.
152 The weather is generally warm, humid and foggy with much cloud, fog and rain but



153 less sunshine. Most rain gathers from July to September, accounting for 80% of total
154 annual precipitation. While in the west plateau, the weather is relatively cool or cold.
155 The climate is featured by a long cold winter, a very short summer and rich sunshine
156 but less rainfall. Thus, annual precipitation shows significant spatial heterogeneity,
157 varying from about 400 mm in the west to 1800 mm in the east and with the average
158 annual precipitation of about 1000 mm. Overall, the high spatial and temporal
159 variability of precipitation with the complex topography makes the study site ideally
160 suitable for the evaluation of satellite-based precipitation estimates.



161
162 Fig. 1 Topography, distribution of rain gauges and geographic location of Sichuan
163 province in China

164 **2.2. Dataset**



165 2.2.1. Rain gauge observations

166 The study region has 156 rain gauge stations, which shows an unevenly distribution
167 with high density in the east and low density in the west (Fig. 1). On average, the
168 cover area of one rain gauge observation is about 3115 km². Daily precipitation data
169 from all the stations for the period 2015–2019 were collected from the China
170 Meteorological Data Service Center (CMDSC, <http://data.cma.cn/>). The data quality
171 was guaranteed based on some strict quality controls, such as manual inspection,
172 outlier check and spatiotemporal consistency verification (Zhao and Yatagai, 2014).
173 After that, the monthly precipitation was produced by aggregating the daily
174 precipitation of rain gauges for each month.

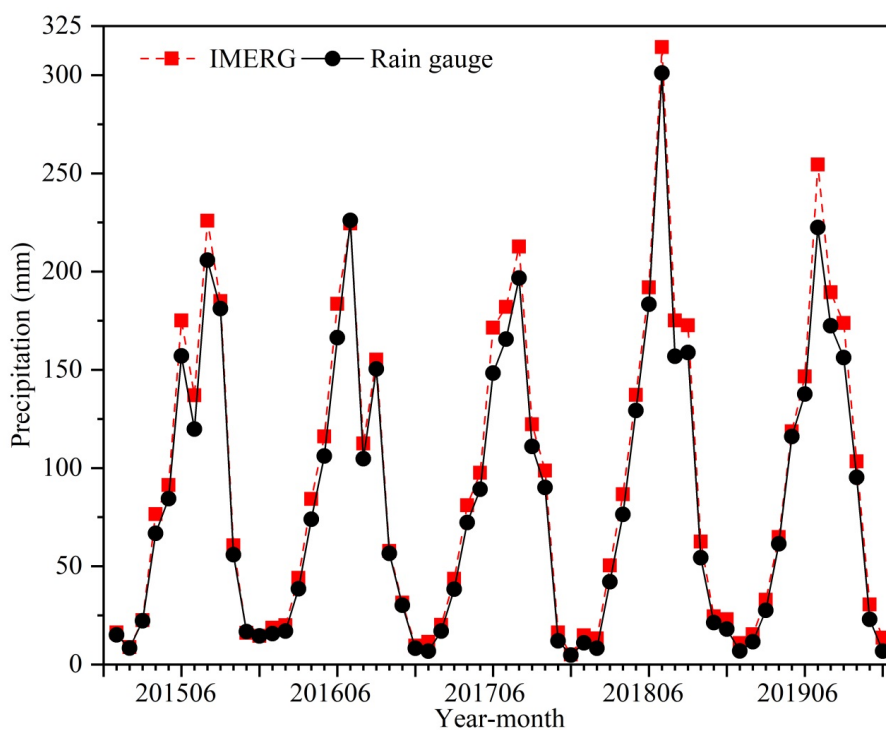
175 2.2.2. Integrated MultisatellitE Retrievals for Global Precipitation Measurement
176 (IMERG)

177 As the successor of TRMM, the National Aeronautics and Space Administration
178 (NASA) and the Japan Aerospace Exploration Agency (JAXA) initiated the
179 next-generation global precipitation observation mission (Hou et al., 2014). The
180 IMERG products were produced by assimilating all microwave and infrared (IR)
181 estimates, together with gauge observations (Huffman et al., 2019). It has the spatial
182 resolution of 0.1° × 0.1° with the coverage from 60°S–60°N. IMERG provides three
183 different products including Early, Late, and Final Runs, which were computed about
184 4 hours, 14 hours, and 3.5 months after observation time, respectively. Due to the
185 incorporation of the Global Precipitation Climatology Centre (GPCC) rain gauge data,
186 IMERG Final Run is more accurate than the others (Lu et al., 2019). Thus, the



187 monthly IMERG V06B Final Run product was adopted in the study. It was
188 downloaded from <https://gpm.nasa.gov/data>.

189 The mean monthly precipitations based on all rain gauges and IMERG during
190 2015-2019 are shown in Fig. 2. Obviously, IMERG has an overestimation in most
191 months and the wettest month is July 2018.




192
193 Fig. 2 Mean monthly precipitation based on rain gauges and IMERG from 2015-2019
194 over Sichuan province

195 2.2.3. Environmental variables

196 The Moderate Resolution Imaging Spectroradiometer (MODIS) onboard the
197 NASA's Terra and Aqua platforms provides plenty of products in global dynamics,
198 oceans and land processes. The MODIS monthly NDVI with the resolution of 1 km



199 (MOD13A3) from 2015 to 2019 was used in the study and downloaded from
200 International Scientific and Technical Data Mirror Site, Computer Network
201 Information Center of the Chinese Academy of Sciences (<http://www.gscloud.cn/>).
202 MODIS 8-day LST with the resolution of 1 km (MOD11A2) from 2015 to 2019 was
203 obtained from <https://ladsweb.modaps.eosdis.nasa.gov> and then temporally averaged
204 into the monthly LST products. In the study, the daytime LST (LST_D), nighttime LST
205 (LST_N) and the difference between daytime and nighttime LSTs (LST_{D-N}) at the
206 monthly scale were used.

207 The Shuttle Radar Topography Mission (SRTM) cooperated by the National
208 Geospatial Intelligence Agency (NGA) and the National Aeronautics and Space
209 Administration (NASA)  provides high resolution DEMs. The SRTM DEM with the
210 spatial resolution of 90 m was downloaded from <http://srtm.csi.cgiar.org/> and then
211 resampled to 1 km by the pixel averaging method. Moreover, topographical factors
212 including slope, aspect and terrain relief (Chen et al., 2020a) were extracted from the
213 SRTM DEM in ArcGIS 10.3.

214 The detailed information of the datasets used in the study is shown in Table 1.

215 Table 1 Datasets used in the study

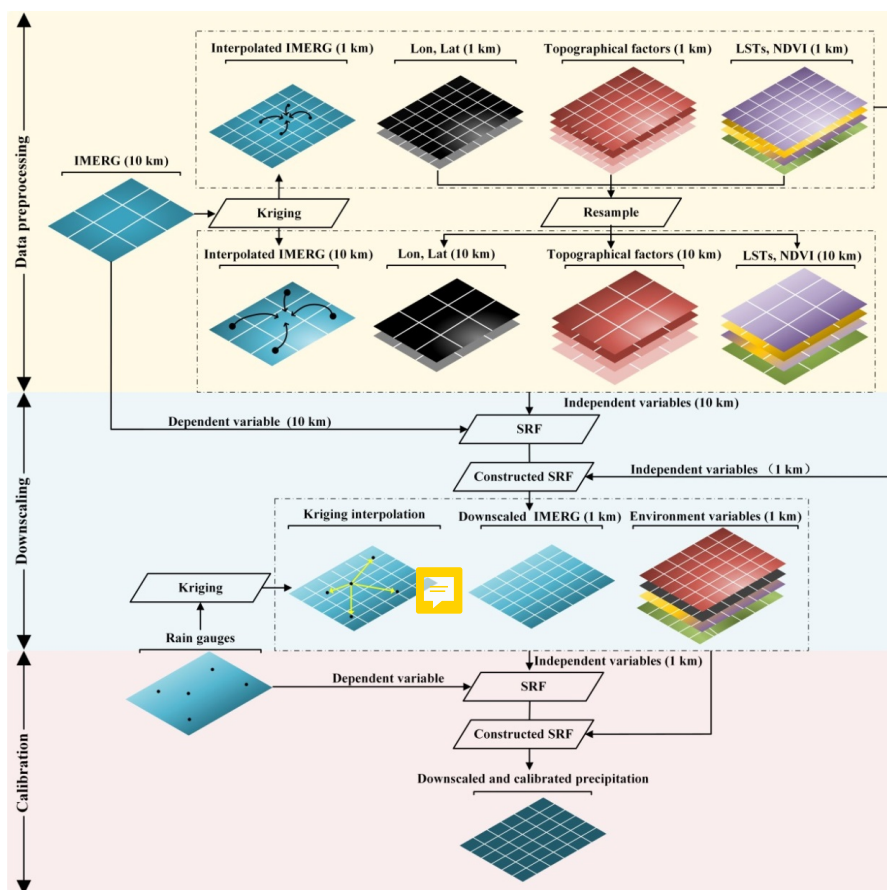
Data Type	Product	Spatial resolution	Temporal resolution	Source
Meteorological data	GPM IMERG	10 km	Monthly	https://gpm.nasa.gov/data
	Rain gauge observations	-	Daily	http://data.cma.cn/
Land surface	SRTM DEM	30 m	-	http://srtm.csi.cgiar.org/



data	slope, aspect, terrain relief	30 m	-	Derived from SRTM DEM
	NDVI	1 km	Monthly	http://www.gscloud.cn/
	LST	1 km	8-days	https://ladsweb.modaps.eosdis.nasa.gov

216 **3. Methodology**

217 The flowchart of our method is demonstrated in Fig. 3, which includes three main
218 stages: (i) data processing; (ii) IMERG downscaling and (iii) downscaled IMERG
219 calibration. It is noted that downscaling before calibration is to avoid scale mismatch
220 between satellite-based areal precipitation and gauge-based point measurements.



221

222

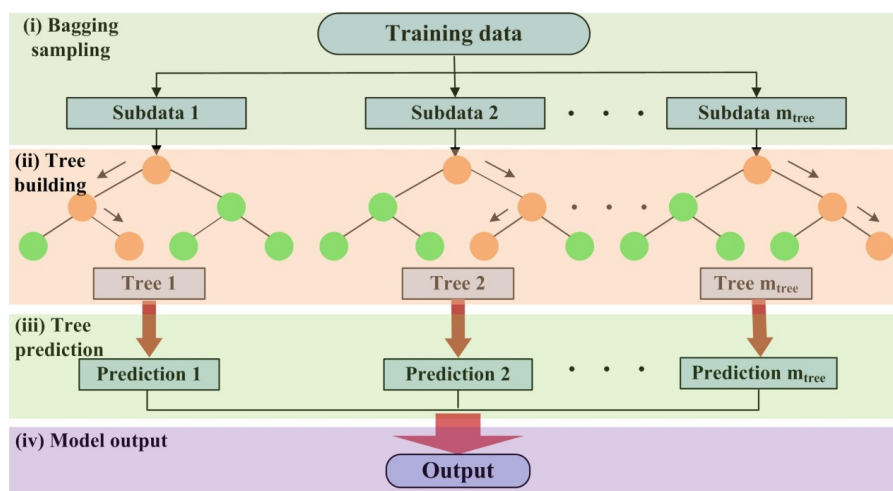
Fig. 3 Flowchart of the proposed method

223 3.1. Random Forest

224 RF is an ensemble of several tree predictors such that each tree relies on a random
225 and independent selection of features but with the same distribution (Breiman, 2001).
226 Specifically, each decision tree is constructed by randomly collecting some training
227 data with replacement while the other is used to assess the tree (sample bagging).
228 Moreover, while constructing each tree, only a random subset of features is selected at
229 each decision node (feature bagging). In the end, the majority vote for classification



230 or the average prediction of all trees for regression is used to obtain the final output.
231 Meanwhile, RF can evaluate the relative importance of the predictors by means of
232 out-of-bag (OOB) observations. With the OOB error, the importance of each variable
233 can be ranked. Many benchmarking researches have proven that RF is one promising
234 ML technique currently available (Hengl et al., 2018). The general framework of RF
235 is shown in Fig. 4.



236
237

Fig. 4 General framework of RF

238 3.2. Spatial Random Forest (SRF)



239 In essence, the classical RF is a non-spatial statistical technique for spatial
240 prediction since it neglects sampling locations and general sampling pattern (Hengl et
241 al., 2018). This can potentially cause sub-optimal estimations, especially when the
242 spatial autocorrelation between dependent variables is high. To this end, a spatial RF
243 is proposed in this paper. The general formulation of SRF is as follows:



244
$$\hat{p}(s_0) = f(\mathbf{X}_s, \mathbf{X}_{ns}) + e$$

245 where \hat{p} is the estimated precipitation at the location s_0 , e is the fitting residual, and \mathbf{X}_s
246 and \mathbf{X}_{ns} are the spatial and non-spatial covariates, respectively.

247 In addition to spatial coordinates, one spatial covariate (X_s) is estimated to account
248 for the spatial autocorrelation between neighboring precipitation measurements, i.e.

249
$$X_s(s_0) = \sum_{i=1}^n w_i z(s_i)$$

250 where $z(s_i)$ is the i th neighboring precipitation data at the unknown point s_0 , w_i is its
251 weight and n is the number of known data used for the estimation.

252 In previous studies (Li et al., 2017; Zhang et al., 2021), the inverse distance weights
253 (IDW) were commonly used. However, the IDW method only resorts to the spatial
254 distance between the estimated point and the adjacent known points, and does not
255 consider the spatial autocorrelation between the known points. To overcome this
256 limitation, the ordinary kriging-based variogram is adopted to estimate the
257 interpolation weights, which are obtained by solving the following linear system:

258
$$\begin{pmatrix} \gamma(\mathbf{x}_1 - \mathbf{x}_1) & \cdots & \gamma(\mathbf{x}_1 - \mathbf{x}_n) & 1 \\ \vdots & \ddots & \vdots & \vdots \\ \gamma(\mathbf{x}_n - \mathbf{x}_1) & \cdots & \gamma(\mathbf{x}_n - \mathbf{x}_n) & 1 \\ 1 & \cdots & 1 & 0 \end{pmatrix} \begin{pmatrix} w_1 \\ \vdots \\ w_n \\ \mu \end{pmatrix} = \begin{pmatrix} \gamma(\mathbf{x}_1 - \mathbf{x}_0) \\ \vdots \\ \gamma(\mathbf{x}_n - \mathbf{x}_0) \\ 1 \end{pmatrix}$$

259 where μ is Lagrange parameter and $\gamma(\cdot)$ is the semivariogram.

260 It can be concluded that the variogram-based weights consider the spatial
261 autocorrelation not only between the adjacent known points but also between the
262 known points and the interpolated point (Berndt and Haberlandt, 2018). Thus, it
263 seems more accurate than IDW. In practice, the experimental semivariogram is



264 estimated from sample data with the following equation (Goovaerts, 2000):

$$265 \quad \hat{\gamma}(h) = \frac{1}{2n} \sum_{i=1}^n (z(\mathbf{x}_i) - z(\mathbf{x}_i + h))^2$$

266 where n is the number of data pairs with the attribute z separated by distance h .

267 Generally, a theoretical semivariogram model was fitted to the experimental values
268 to obtain the semivariogram at any h . There are four commonly used theoretical
269 semivariogram models: the spherical, Gaussian, exponential, and power models. In
270 our study, the spherical model was used since it shows better results than the others in
271 the experiments.

272 3.3. Working procedure of the proposed method

273 The detailed steps of the proposed method are as follows (Fig. 3):

274 (1) Each pixel value of the 10 km IMERG was re-estimated by ordinary kriging
275 interpolation with its k nearest neighbors (e.g. $k=8$) to obtain the interpolated
276 IMERG (termed as I_s^{10}) the 10 km IMERG was interpolated by kriging to
277 obtain the interpolated 1 km IMERG (I_s^{1km}), and the gauge observations are
278 interpolated by kriging to produce the 1 km precipitation map (P_s^{1km}). It is noted
279 that the semivariogram model cannot be accurately estimated from the sparse
280 gauge measurements. Hence, it is difficult to accurately show the spatial
281 autocorrelation between the precipitation estimates. Motivated by the idea of Chen
282 et al. (2020c) that the satellite-based precipitation can show the spatial distribution
283 of precipitation, we used the satellite-based precipitation to estimate the
284 experimental semivariogram for interpolating gauge measurements.



285 (2) The negative NDVI values were excluded from the original data, which mainly
286 belong to snow and water bodies in the study site. The removed ones were
287 estimated by kriging with their neighbors, which can avoid much information loss.

288 (3) The 1 km environmental variables \mathbf{X}_{ns}^{1km} (i.e. NDVI, LST_D, LST_N, LST_{D-N}, DEM,
289 slope, aspect, terrain relief, latitude and longitude) were resampled to the 10 km
290 resolution \mathbf{X}_{ns}^{10km} by the pixel averaging method.

291 (4) The relationship between \mathbf{X}_{ns}^{10km} , I_s^{10km} and the 10 km IMERG ($IMERG^{10km}$)
292 was constructed by SRF:

$$293 \quad IMERG(s_0) = f_{\text{downscale}}(I_s^{10km}(s_0), \mathbf{X}_{ns}^{10km}(s_0)) + e^{10km}(s_0)$$

294 where e is the fitting residual.

295 (5) The IMERG was downscaled to 1 km (\hat{D}^{1km}) by the constructed relationship in
296 step (4) with \mathbf{X}_{ns}^{1km} and I_s^{1km} :

$$297 \quad \hat{D}^{1km} = f_{\text{downscale}}(I_s^{1km}, \mathbf{X}_{ns}^{1km})$$

298 (6) The relationship between the 1 km predictors and the gauge observations (G) are
299 constructed by SRF:

$$300 \quad G(s_0) = f_{\text{calibrate}}(P_s^{1km}(s_0), \hat{D}^{1km}(s_0), \mathbf{X}_{ns}^{1km}(s_0)) + e^{1km}(s_0)$$

301 (7) The 1 km high quality precipitation data (C^{1km}) are produced based on the
302 constructed relationship in step (6):

$$303 \quad C^{1km} = f_{\text{calibrate}}(P_s^{1km}, \hat{D}^{1km}, \mathbf{X}_{ns}^{1km})$$

304 In our study, residual correction was ignored during downscaling and calibration,
305 since many previous studies (Karbalaye Ghorbanpour et al., 2021; Lu et al., 2019)
306 demonstrated that residual correction on the ML-based technique decreased the



307 prediction accuracy.

308 **3.4. Comparative methods**

309 In the study, the performance of our method was comparatively assessed using
310 three manners. Firstly, we compared the results of the proposed method with those of
311 the classical methods including GWR, RF and BPNN. Secondly, our methodology
312 was compared with two classical frameworks: (i) the IMERG was downscaled by the
313 bilinear interpolation and then calibrated by SRF (termed as Bi-SRF), and (ii) the
314 IMERG was downscaled by SRF and then calibrated by GDA (termed as SRF-GDA).
315 Thirdly, our monthly-based estimation method was compared with the annual-based
316 SRF fraction disaggregation method (termed as SRFdis). Finally, the results of our
317 method were compared with that from ordinary kriging interpolation only on gauge
318 measurements (termed as kriging). Overall, the proposed method was compared with
319 seven classical methods in our study, including GWR, RF, BPNN, Bi-SRF, SRF-GDA,
320 SRFdis and kriging.

321 Note that the parameters of all the methods were tuned based on the trial-and-error
322 scheme under the l -fold cross validation technique (An et al., 2007). Specifically, all
323 gauge measurements were first divided into l folds. The prediction function was
324 trained using $l-1$ folds, and the remainder was used for validation. The process is
325 repeated l times until all folds were used for validation. Here, we set $l=10$. For each
326 group of specified parameters, the 10-fold cross validation was repeated for one time,
327 and the optimized parameters correspond to the minimized fitting error. Thus, the



328 overfitting problem could be avoided.

329 **3.5. Accuracy measures**

330 Three accuracy measures were adopted in the quantitative accuracy evaluation,
331 including root mean square error (RMSE), mean absolute error (MAE) and correlation
332 coefficient (CC) (Jing et al., 2016; Sharifi et al., 2019). They are respectively
333 expressed as

$$334 \quad RMSE = \sqrt{\frac{1}{n} \sum_{i=1}^n (E_i - O_i)^2}$$

$$335 \quad MAE = \frac{\sum_{i=1}^n |E_i - O_i|}{n}$$

$$336 \quad CC = \frac{\sum_{i=1}^n (E_i - \bar{E})(O_i - \bar{O})}{\sqrt{\sum_{i=1}^n (E_i - \bar{E})^2} \times \sqrt{\sum_{i=1}^n (O_i - \bar{O})^2}}$$

337 where n is the number of testing stations, E_i and O_i are the estimated and observed
338 precipitations at station i , respectively.

339 Generally, CC is used to measure the consistency between the estimated and
340 observed precipitations, while RMSE and MAE can assess the absolute deviation
341 between the estimated and observed values.

342 **4. Results and analysis**

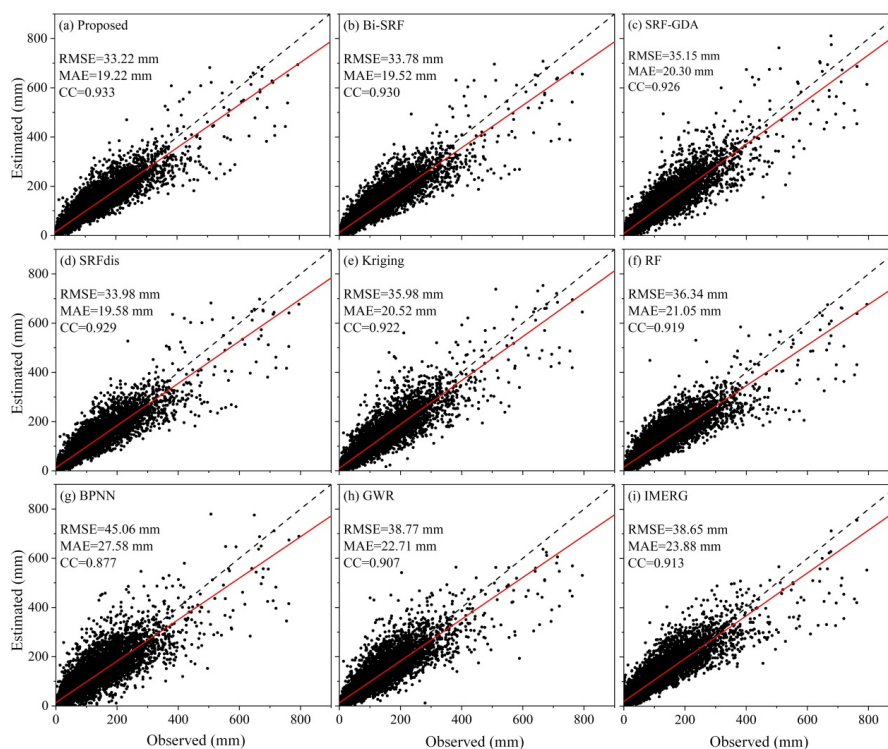
343 We analyzed the results of the proposed method and the other methods on different
344 temporal scales including monthly, seasonal and annual ones, where the latter two



345 scales were averagely computed from the monthly one.

346 **4.1. Monthly scale**

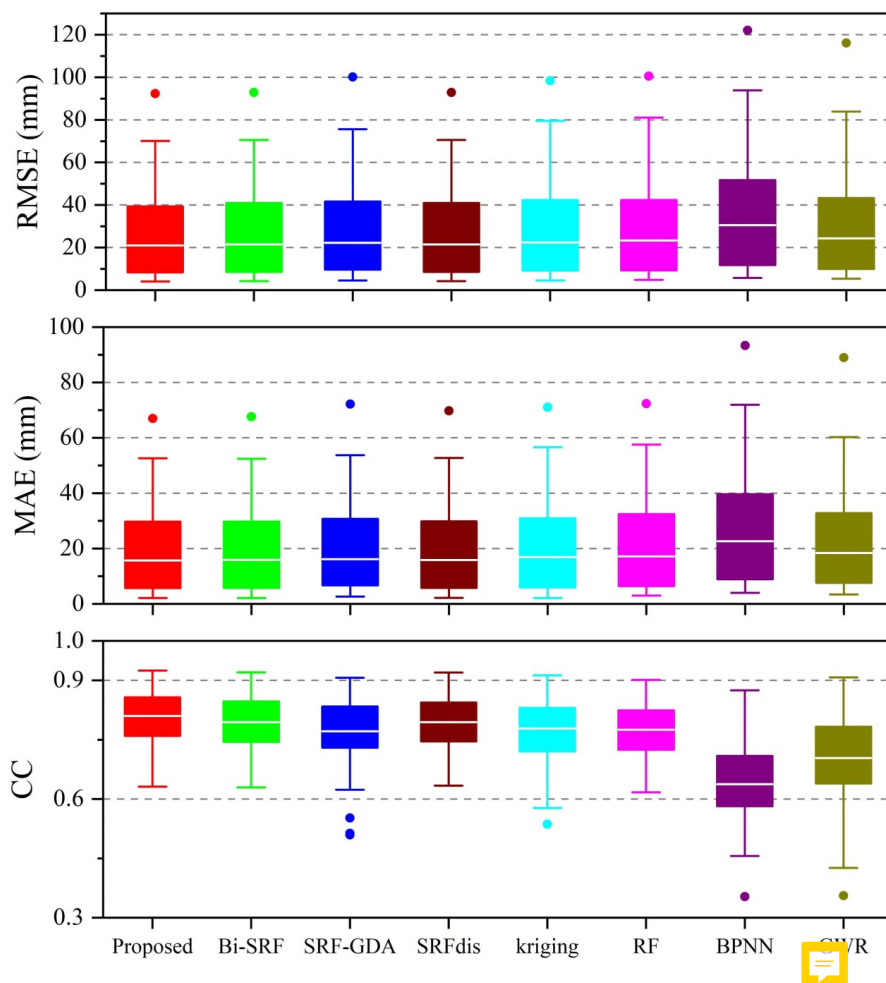
347 Fig. 5 illustrates the scatterplots between the predicted and observed precipitations
348 on a monthly scale from 2015 to 2019. Results demonstrate that regardless of
349 accuracy measures, BPNN and GWR produce worse results than the original IMERG.
350 This is mainly owed to the complex relationship between the precipitation and the
351 predictors, which was not accurately captured by the two methods. RF performs better
352 than IMERG, yet worse than kriging. By contrast, the four SRF-based methods
353 including the proposed method, Bi-SRF, SRF-GDA and SRFdis outperform the other
354 methods. This reflects the significant effect of spatial autocorrelation between the
355 gauge measurements on capturing the complex predictors-precipitation relationship.
356 Moreover, the proposed method with the RMSE, MAE and CC of 33.22 mm, 19.22
357 mm and 0.933 produces the best result. Thus, it can be concluded that (i) SRF-based
358 downscaling and calibration is more effective than bilinear downscaling (Bi-SRF) and
359 GDA-based calibration (SRF-GDA) and (ii) there is no obvious time latency for
360 vegetation response to precipitation in the study site, since the proposed method is
361 slightly more accurate than SRFdis.



362

363 Fig. 5 Scatterplots between the estimated and the observed precipitation on a monthly
364 scale from 2015 to 2019

365 Fig. 6 shows the boxplots of the four accuracy measures. Obviously, BPNN obtains
366 the poorest results, with the median RMSE, MAC and CC of 30.48 mm, 22.66 mm
367 and 0.64, respectively. It is followed by GWR, RF and kriging. The accuracy rank is
368 consistent with that shown in Fig. 5. The four methods based on SRF seem more
369 accurate than the classical methods. SRFdis, Bi-SRF and SRF-GDA have the median
370 RMSEs of 21.41, 21.44 and 22.27 mm, respectively, while the proposed method has
371 the value of 21.03 mm. In other words, the proposed method outperforms the other
372 methods, which further highlights the benefit of including spatial autocorrelation
373 information for downscaling and calibration of satellite-based precipitation.



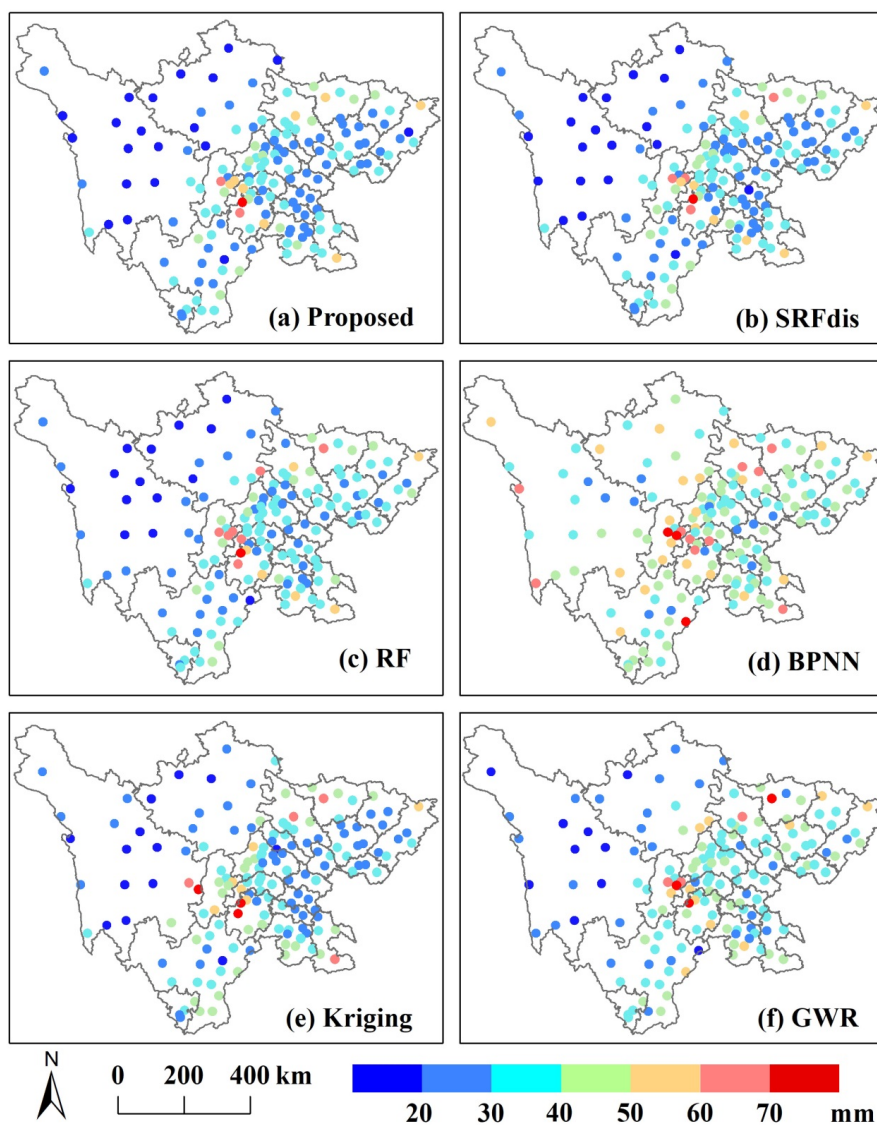
374

375 Fig. 6 Boxplots of RMSE, MAE and CC for the precipitation estimation methods on a
376 monthly scale during 2015-2019

377 Fig. 7 shows the RMSE spatial distribution of all gauge stations for the proposed
378 method, SRFdis, RF, BPNN, kriging and GWR. Overall, the RMSEs tend to be larger
379 in the middle part, since the precipitation is higher in the middle part than in the other
380 parts (Fig. 1). BPNN (Fig. 7d) yields the poorest results, where many stations have the
381 RMSEs greater than 60 mm. It is followed by GWR (Fig. 7f). RF (Fig. 7c) and
382 kriging (Fig. 7e) seem better than GWR and BPNN at most stations. The proposed



383 method (Fig. 7a) and SRFdis (Fig. 7b) are more accurate than the classical methods,
384 especially at the stations in the middle area. Moreover, the proposed method performs
385 better than SRFdis at some stations, such as those in the right-top.



386

387 Fig. 7 RMSE distribution of all gauge stations for the proposed method and some

388

representative methods on a monthly scale during 2015-2019



389 **4.2. Seasonal scale**

390 The estimation errors of all the methods on a seasonal scale (i.e. spring, summer,
391 autumn and winter) are provided in Table 2. Results indicate that regardless of
392 accuracy measures, all methods obtain the best and the worst results in winter and in
393 summer, respectively. This conclusion is consistent with the results yielded by
394 (Baez-Villanueva et al., 2020; Chen et al., 2020c; Zambrano-Bigiarini et al., 2017).
395 This could be due to the facts that (i) winter has the lowest precipitation and summer
396 has the highest one (Fig. 2), and (ii) the large precipitation in summer was caused by
397 complex conditions, like climatic anomaly and encounter of the cold and warm air
398 masses, which cannot be accurately explained by the predictions (Chen et al., 2015).
399 The accuracy rank for all the methods in the four seasons is similar. More specifically,
400 BPNN yields worse results than IMERG in spring, summer and autumn, and a better
401 result in winter. GWR is slightly more accurate than BPNN in the four seasons.
402 Kriging with a similar accuracy to RF obviously outperforms BPNN and GWR. The
403 four SRF-based methods seem more accurate than the classical methods in almost all
404 seasons, expect for SRF-GDA in winter. Moreover, the proposed method consistently
405 performs the best in the four seasons. Taking winter as an example, our method is
406 about 11.44%, 8.59%, 4.77% and 2.89% more accurate than kriging, RF, BPNN and
407 GWR, respectively.

408 Table 2 RMSEs, MAEs and CCs of all the estimation methods on a seasonal scale
409 during 2015-2019 (RMSE: mm; MAE: mm)

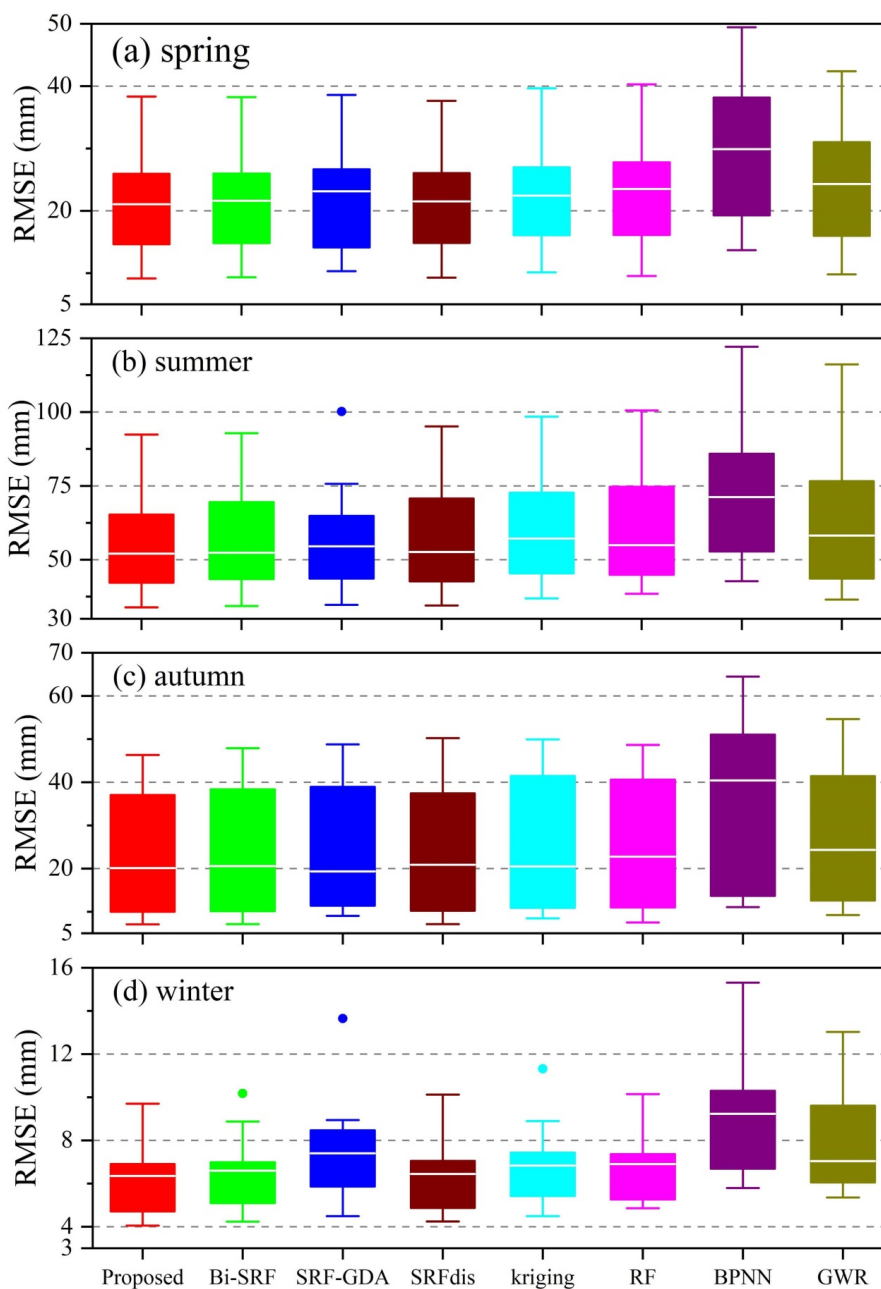


Season	Index	Proposed	Bi-SRF	SRF-GDA	SRFdis	Kriging	RF	BPNN	GWR	IMERG
Spring	RMSE	21.99	22.19	23.03	22.04	23.38	23.67	30.71	25.97	25.97
	MAE	15.36	15.52	15.93	15.48	16.14	16.64	22.48	18.24	19.30
	CC	0.889	0.887	0.882	0.888	0.876	0.870	0.793	0.841	0.855
Summer	RMSE	56.13	57.06	59.27	57.51	61.07	61.83	74.46	65.49	64.46
	MAE	39.92	40.44	41.77	40.63	43.16	43.66	54.55	46.32	47.30
	CC	0.857	0.851	0.845	0.849	0.832	0.824	0.745	0.795	0.818
Autumn	RMSE	27.50	28.06	29.23	28.24	29.49	29.48	39.70	31.63	32.19
	MAE	17.51	17.89	18.53	17.96	18.42	19.25	26.67	20.79	21.98
	CC	0.928	0.925	0.920	0.924	0.918	0.917	0.864	0.902	0.905
Winter	RMSE	6.29	6.54	7.70	6.51	7.01	6.83	9.29	8.11	11.28
	MAE	4.11	4.25	4.97	4.26	4.36	4.65	6.64	5.66	6.93
	CC	0.853	0.839	0.790	0.841	0.823	0.826	0.688	0.735	0.595

410 To further illustrate the distributions of each accuracy measure, the boxplots of
 411 RMSEs, MAEs and CCs in each season are provided in Figs. 8, 9 and 10, respectively.
 412 Obviously, BPNN has the largest accuracy range in the four seasons, indicating its
 413 instability for precipitation estimation. Moreover, it produces the largest median
 414 RMSEs and MAEs with the values of 9.23-71.25 mm and 6.90-55.42 mm,
 415 respectively, and the smallest median CCs with the values of 0.61-0.66. Compared to
 416 BPNN, the RMSEs of RF and GWR are decreased to 6.90-54.92 mm and 7.04-58.17
 417 mm, respectively, MAEs to 4.67-40.10 mm and 5.02-41.48 mm, respectively, while
 418 CCs are increased to 0.76-0.80 and 0.39-0.73, respectively. Kriging performs better

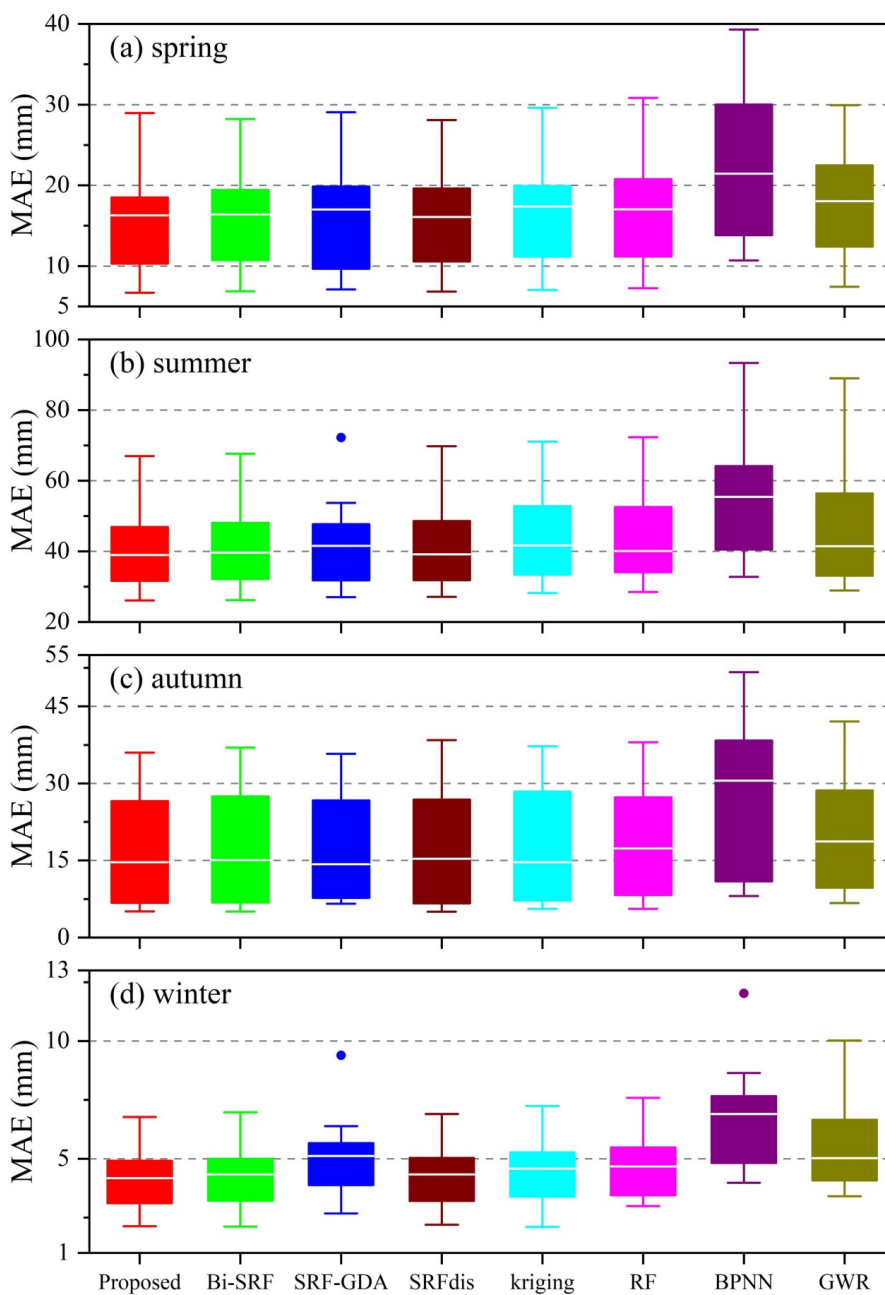


419 than RF and GWR in almost all seasons, except for summer. Except for SRF-GDA,
420 the other SRF-based methods are more accurate than the classical methods. On the
421 whole, the proposed method produces the best results, with the median RMSEs,
422 MAEs and CCs of 6.35-52.08 mm, 4.18-38.94 mm and 0.78-0.84 in the four seasons.



423

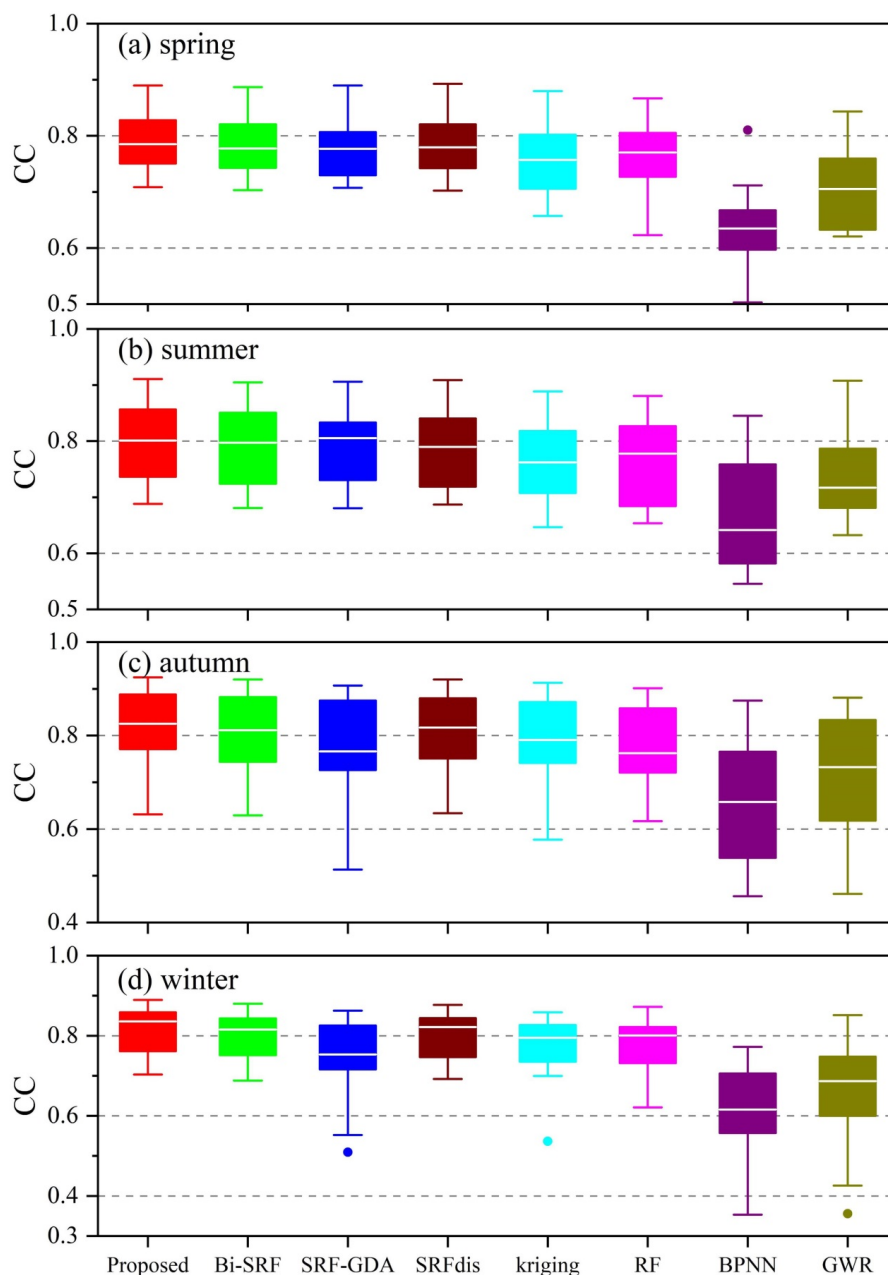
424 Fig. 8 Boxplots of RMSEs of all the methods on the seasonal scale during 2015-2019



425

426

Fig. 9 Boxplots of MAEs of all the methods on the seasonal scale during 2015-2019



427

428

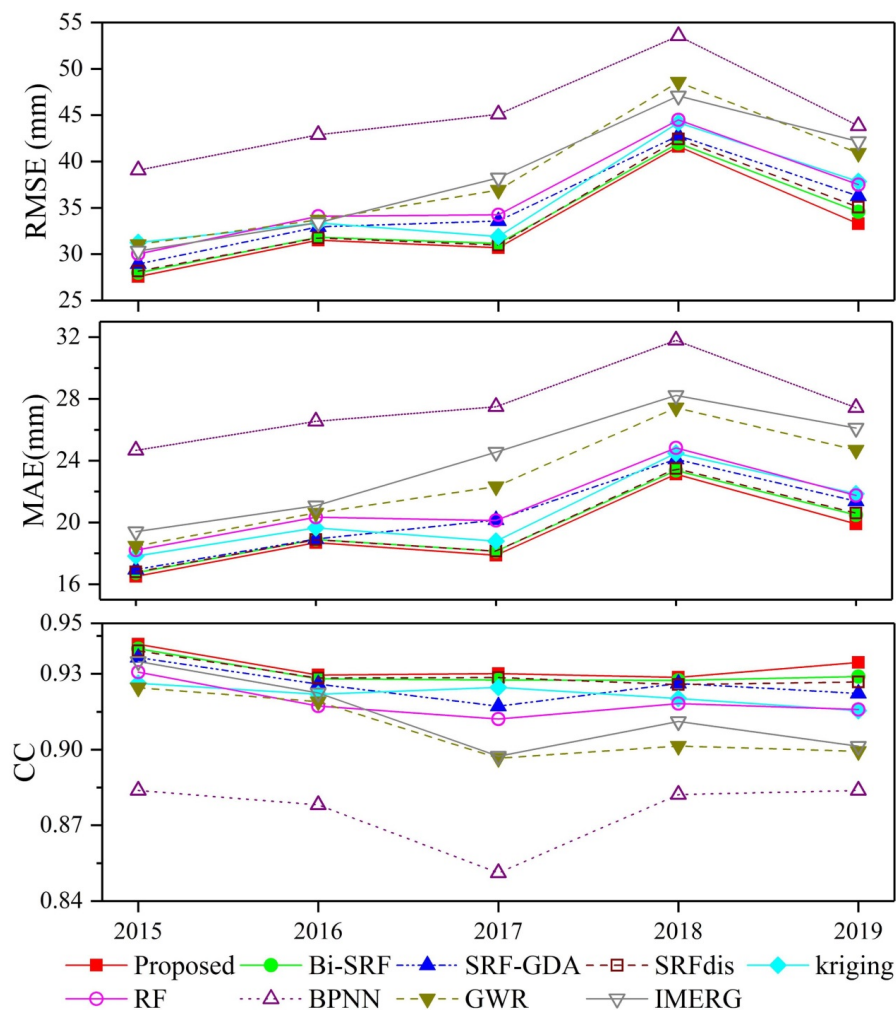
Fig. 10 Boxplots of CCs of all the methods on the seasonal scale during 2015-2019

429

4.3. Annual scale



430 Fig. 11 illustrates the accuracy measures of all the methods on an annual scale from
431 2015 to 2019. Results demonstrate that all methods produce the worst results in 2018.
432 This is because this year has the largest precipitation (Fig. 2). In comparison, BPNN
433 produces the poorest results in all years, which is followed by IMERG and GWR. RF
434 and kriging are consistently more accurate than BPNN, IMERG and GWR, especially
435 in 2017-2019. The proposed method always performs better than the other methods in
436 the five years, which is closely followed by Bi-SRF and SRFdis. SRF-GDA produces
437 worse results than the other SRF-based methods.



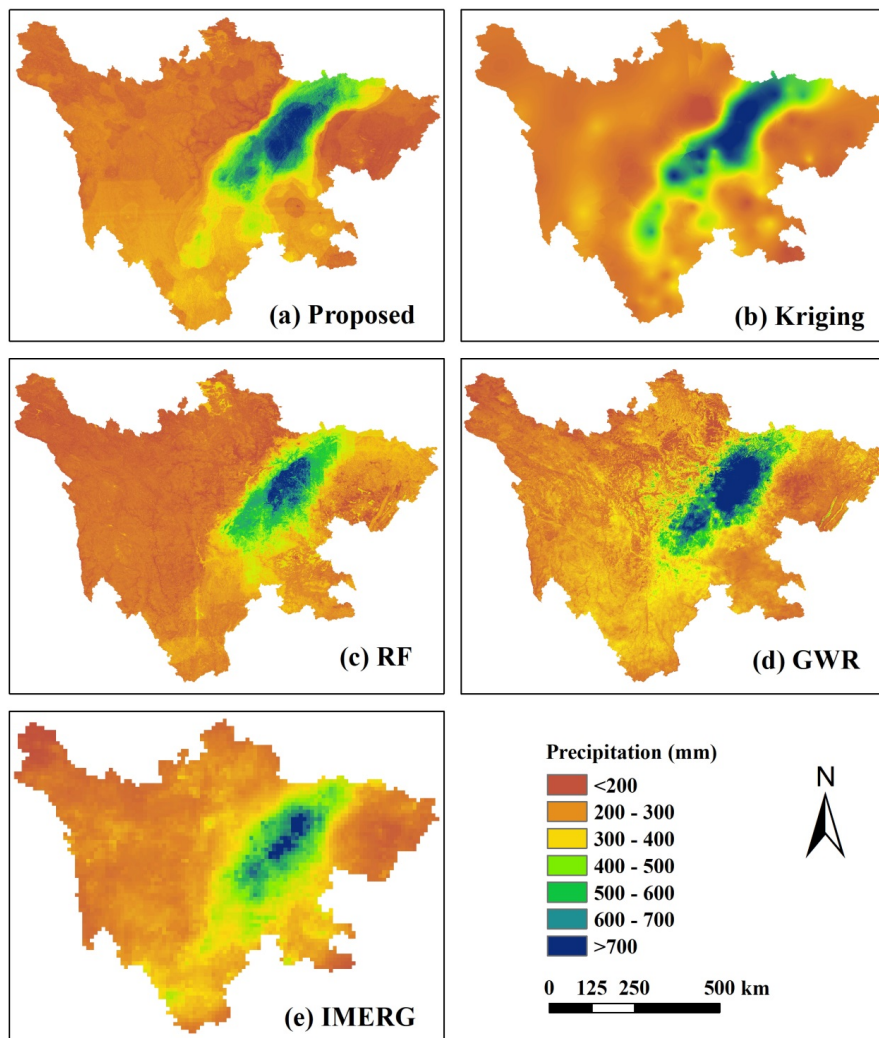
438

439 Fig. 11 Accuracy measures of all the methods on an annual scale from 2015 to 2019

440 Since the wettest month was July 2018 (Fig. 2), it was taken as an example to show
 441 the precipitation estimates of the proposed method and some classical methods.
 442 Results (Fig. 12) indicate that all the estimated precipitation maps have a similar
 443 spatial distribution and pattern to IMERG, yet the former have more detailed
 444 information than the latter due to the inclusion of the high-resolution predictors.
 445 However, there exist some differences between the methods. Specifically, the kriging



446 map (Fig. 12b) loses many details of spatial precipitation patterns. This is expected as
447 it only uses ground measurements for the interpolation. RF (Fig. 12c) shows obvious
448 unnatural discontinuity. GWR (Fig. 12d) suffers from more variations and fractions
449 compared with neighbors. In comparison, the proposed method (Fig. 12a) produces a
450 good precipitation map.



451

452 Fig. 12 Downscaled and calibrated precipitation comparison between the proposed



453 method and some representative methods on the wettest month

454 **5. Discussion**

455 For downscaling and calibration of satellite-based precipitation, the three most
456 important factors are model, predictors and temporal scale used for constructing
457 predictors-precipitation relationship (Chen et al., 2020b). Thus, they should be
458 carefully selected to produce accurate precipitation data.

459 **5.1. Model**

460 In previous studies, the most commonly adopted model is GWR (Chen et al., 2015;
461 Xu et al., 2015), since it has the merit of taking the spatial variation between the
462 predictors and precipitation into account. However, the performance of GWR
463 seriously depends on the density of rain gauge stations, and large interpolation errors
464 can be found in areas with sparse gauge stations and complex terrain characteristics
465 (Lu et al., 2019). Ma et al. (2017) indicated that GWR-based downscaled TRMMs
466 before and after residual correction for the period 2000 to 2013 at an annual scale are
467 less accurate than the original TRMM over the Tibet Plateau. Karbalaye Ghorbanpour
468 et al. (2021) showed that GWR has poorer downscaling results than the original
469 TRMM for 2012 and 2013 on an annual scale over Lake Urmia Basin. Our results
470 demonstrated that on a monthly scale (Fig. 5), GWR produces worse results than the
471 original IMERG, with the RMSE, MAE and CC values of 38.77 mm, 22.71 mm and
472 0.907, respectively. On a seasonal scale (Table 1), GWR is less accurate than IMERG



473 in summer, with the RMSE, MAE and CC values of 65.49 mm, 46.32 mm and 0.795,
474 respectively. On an annual scale (Fig. 11), compared to IMERG, the performance of
475 GWR is unsatisfactory in terms of CC. Moreover, the precipitation map of GWR
476 shows some larger values compared to their neighbors (Fig. 12d).

477 In contrast, the ML methods including RF and SRF are always more accurate than
478 GWR due to their merits for handling the complex nonlinear predictors-precipitation
479 relationship. This conclusion agrees well with previous studies (Karbalaye
480 Ghorbanpour et al., 2021; Sachindra et al., 2018). In addition, the ML methods do not
481 require residual correction (Jing et al., 2016; Shi et al., 2015). However, as a statistical
482 tool, the classical ML methods neglected the spatial autocorrelation between the
483 gauge measurements. Thus, a spatial RF (SRF) with the consideration of the spatial
484 autocorrelation information was constructed. SRF was used in both downscaling and
485 calibration in our study, where the original IMERG and the gauge data were
486 interpolated to produce input predictors for the first and second stages, respectively.
487 The results on the three scales demonstrated the higher accuracy of SRF than RF (see
488 Figs. 5-11, Table 1). Note that although kriging interpolation based on only gauge
489 measurements is more accurate than IMERG, BPNN and GWR, its precipitation map
490 is so smooth that many detailed precipitation patterns are lost (Fig. 12b).



491 **5.2. Environmental predictors**

492 NDVI, latitude, longitude and DEM-based parameters were commonly adopted
493 environmental variables for estimating precipitation (Shi et al., 2015). However,

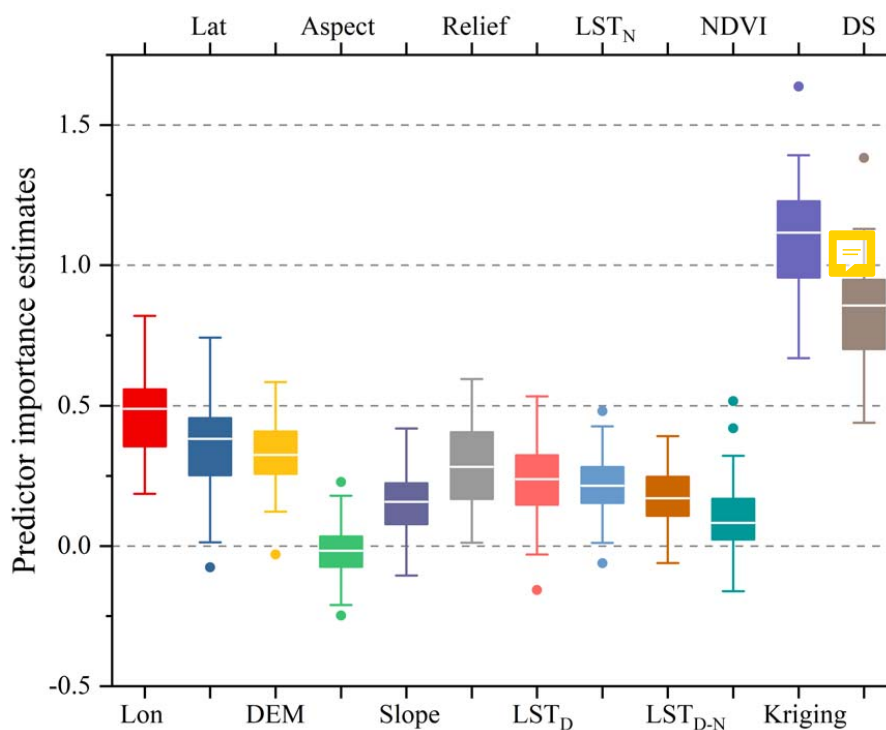


494 satellite-based precipitation across regions with no relationship with NDVI and DEM
495 could not be estimated. For example, in barren or snow areas, the precipitation does
496 not influence NDVI due to the sparse distribution of vegetation (Xu et al., 2015).
497 Jing et al. (2016) indicated that the downscaled models including LST features (LSTs)
498 performed better those without LSTs. Thus, in addition to NDVI and DEM-related
499 parameters, daytime LST (LST_D), nighttime LST (LST_N), and difference between
500 day and night LSTs (LST_{D-N}) were also used in our study.

501 Based on RF (Breiman, 2001), the relative importance of each predictor (i.e.
502 predictor importance estimate) is shown in Fig. 13. Results show that precipitation
503 from kriging interpolation has the most importance, which indicates the significance
504 of the spatial autocorrelation between gauge measurements. Kriging estimation is
505 followed by downscaled precipitation. The three LSTs also have a great impact on
506 the precipitation estimation, where LST_D seems more important than LST_N and
507 LST_{D-N} . NDVI has a slight effect on the precipitation, which ranks last but one. This
508 might be due to the fact that NDVI is influenced by both precipitation and
509 temperature in the study site, and the low temperature above certain elevations
510 hinders the vegetation growth. Motivated by this idea, Wang et al. (2019) first
511 removed the influence of temperature on NDVI, and then used the processed NDVI
512 for downscaling TRMA in Qilian Mountains. Different from the aforementioned
513 scheme, we took both LSTs and NDVI as the predictors, and then the complex
514 predictors-precipitation relationship was captured by RF based on its powerful
515 learning ability. Among the 12 predictors, aspect has the least importance. This



516 conclusion was also obtained by Ma et al. (2017) for downscaling TMPA 3B43 V7
517 data over the Tibet Plateau. Compared to aspect, DEM and terrain slope seem more
518 important.




519
520 Fig. 13 Predictor importance estimates (Lat: latitude; Lon: longitude; DS: downscaled
521 precipitation; kriging: interpolated precipitation based kriging on gauge data)

522 5.3. Temporal scale

523 Temporal scale has a great effect on the selection of predictors for precipitation
524 estimation. There is a debate on whether NDVI should be taken as a predictor for
525 downscaling and calibration of monthly precipitation. Some (Duan and Bastiaanssen,
526 2013; Immerzeel et al., 2009) argued that NDVI cannot be used for monthly



527 precipitation estimation since the response of NDVI to precipitation usually delayed
528 for two or three months. Hence, one effective solution is to perform downscaling at
529 the annual scale, and then use the monthly fractions derived from the original
530 precipitation data to disaggregate the annual precipitation to the monthly one (i.e.
531 annual-based fraction disaggregation) (Duan and Bastiaanssen, 2013). However, some
532 (Brunsell, 2006; Chen et al., 2020c; Lu et al., 2019; Xu et al., 2015) stated that the
533 precipitation-NDVI relationship is hardly time-delayed, since vegetation could
534 influence precipitation by adjusting temperature and air moisture during the growing
535 seasons. Thus, it is possible to estimate precipitation with NDVI at the monthly scale.
536 In our study, we found that the proposed method on the monthly scale is slightly more
537 accurate than that on the annual scale (i.e. SRFdis) in all seasons (see Figs. 8-10),
538 indicating that NDVI could be used for monthly precipitation estimates in the study
539 site. 

540 ***5.4. Easy-to-use feature***

541 Since the classical RF does not consider the spatial information in the modeling
542 process, Hengl et al. (2018) proposed an improved RF for spatial estimation, where
543 the buffer distances from the point-based measurements were taken as the predictors.
544 Motivated by this idea, Baez-Villanueva et al. (2020) presented a RF-based method
545 (RF-MEP) for merging satellite precipitation products and rain gauge measurements,
546 where the spatial distances from all rain gauges to the grid cells in the study site were
547 used as the variables. RF-MEP performed better than all precipitation products and



548 some merging methods. However, as stated by Baez-Villanueva et al. (2020),
549 RF-MEP has a huge computational cost, since the number of extra input features
550 equals to that of gauge measurements. Moreover, RF-MEP ignored the spatial
551 autocorrelation between the gauge measurements. In comparison, our SRF only
552 requires one extra feature that is estimated by kriging interpolation on the
553 precipitation measurements. Compared to the buffer distance layers, it is much more
554 computationally effective. Moreover, with the variogram-based kriging interpolation,
555 the spatial autocorrelations between the gauge measurements and between the
556 estimated precipitation and gauge measurements are taken into account. Thus, the
557 aforementioned features make our method accurate, effective and easy-to-use.

558 Recently, Georganos et al. (2019) proposed a geographical RF to overcome spatial
559 heterogeneity in remote sensing and population modelling. The geographical RF is
560 essentially a local interpolation method, where only the n nearest observations around
561 the interpolated point is used. However, this kind of methods has the tendency to
562 produce discontinuity maps due to the local interpolation nature (Chen and Li, 2019).
563 Moreover, the global information inherent in the dataset cannot be used, which might
564 result in biased results. In comparison, our method with the aforementioned features is
565 highly recommended.

566 **5.5. Further researches**

567 In the further studies, we will focus on the following directions. Firstly, other land
568 surface variables such as soil moisture (Brocca et al., 2019; Fan et al., 2019), and



569 meteorological conditions such as cloud properties (Sharifi et al., 2019) could be
570 adopted to enhance the predictors-precipitation relationship, thereby further
571 improving IMERG quality. Secondly, the correction of satellite-based precipitation on
572 higher-temporal scales (e.g. daily or hourly) is challenging and valuable (Chen et al.,
573 2020b; R. Lima et al., 2021; Sun and Lan, 2021; Wu et al., 2020). Whether our
574 method could be applied on these scales might need validation. Thirdly, in our
575 experiments, all rain gauge measurements were used to improve the quality of
576 satellite-based precipitation. However, it is generally accepted that sample density has
577 a significant effect on the accuracy of the classical calibration methods
578 (Baez-Villanueva et al., 2020; Bai et al., 2019; Lin and Wang, 2011; Wang and Lin,
579 2015; Zhang et al., 2021). Thus, its influence on the results of our method should be
580 quantitatively assessed, thereby determining the most suitable gauge density in
581 different hydrological applications. Finally, numerous satellite-based precipitation
582 products have been available, and each one has its shortcomings and advantages for
583 the capture of spatial precipitation patterns (Baez-Villanueva et al., 2020; Chen et al.,
584 2020c). Thus, the fusion of multiple precipitation products based on our methodology
585 is a promising alternative to improve the quality of precipitation data. Thus, its
586 performance requires further assessment.

587 **6. Conclusions**

588 To enhance the resolution (from 0.1° to 1 km) and accuracy of the monthly IMERG
589 V06B Final Run product, a spatial RF (SRF)-based downscaling and calibration



590 method is proposed in this paper. The merits of the proposed method are twofold: (i)
591 SRF takes the spatial autocorrelation between the precipitation measurements into
592 account when constructing the predictors-precipitation relationship and (ii) the SRF
593 model is used not only in downscaling but also in calibration of IMERG, with the
594 incorporation of some precipitation-related high-resolution variables. The
595 performance of the proposed method was compared with those of seven methods
596 including GWR, RF, BPNN, Bi-SRF, SRF-GDA, SRFdis and kriging for enhancing
597 the quality and resolution of monthly IMERG across Sichuan province, China from
598 2015 to 2019. The main findings and conclusions can be summarized as follows:

599 (1) The SRF-based methods including the proposed method, Bi-SRF, SRF-GDA and
600 SRFdis are more accurate than the classical methods on all temporal scales.
601 Moreover, the proposed method ranks the first, indicating that SRF-based
602 downscaling and calibration is more promising than bilinear-based downscaling
603 and GDA-based calibration.

604 (2) The comparison between the monthly-based and annual-based estimation
605 demonstrates that there is no statistically significant difference between them,
606 indicating that NDVI can be used for monthly precipitation estimation in the study
607 site.

608 (3) Kriging outperforms the original IMERG, BPNN and GWR in terms of RMSE,
609 MAE and CC. However, its interpolation map suffers from serious loss of spatial
610 variation of precipitation, since it only uses the gauge measurements.

611 (4) Based on the variable importance assessment of RF, the precipitation interpolated



612 by kriging on the gauge measurements is the most important variable, whereas
613 terrain aspect is the least one.

614 Overall, the proposed methodology is general, robust, accurate and easy-to-use,
615 since its promising performance in the study area with an obvious heterogeneity in
616 terrain morphology and precipitation. Thus, it can be easily applied to other regions,
617 where high resolution and accurate precipitation data is urgently required.

618 **Data availability**

619 The gauge data are from the China Meteorological Data Service Center
620 (<http://data.cma.cn>, last access: January 2021). The GPM data are from
621 <https://gpm.nasa.gov/data> (last access: January 2021). The GPM data are from
622 <http://srtm.csi.cgiar.org/> (last access: January 2021). The MOD13A3 data are from
623 <http://www.gscloud.cn/> (last access: January 2021). The MOD11A2 data are from
624 <https://ladsweb.modaps.eosdis.nasa.gov> (last access: January 2021).

625 **Declaration of Competing Interest**

626 The authors declare that they have no known competing financial interests or
627 personal relationships that could have appeared to influence the work reported in this
628 paper.

629 **Author contributions**

630 CF and YY conceived the idea, and acquired the project and financial support. BJ
631 conducted the detailed analysis. CF contributed to the writing and revisions.



632 **Competing interests**

633 The authors declare that they have no conflict of interest.

634 **Acknowledgement**

635 This work was supported by the National Natural Science Foundation of China
636 (Grant No. 41804001), Shandong Provincial Natural Science Foundation, China
637 (Grant No. ZR2020YQ26, ZR2019MD007, ZR2019BD006), A Project of Shandong
638 Province Higher Educational Youth Innovation Science and Technology Program
639 (Grant No. 2019KJH007), Shandong Provincial Key Research and Development
640 Program (Major Scientific and Technological Innovation Project) (Grant No.
641 2019JZZY010429) and by the Scientific Research Foundation of Shandong
642 University of Science and Technology for Recruited Talents (Grant No.
643 2019RCJJ003).

644 **References**

- 645 An, S., Liu, W., Venkatesh, S., 2007. Fast cross-validation algorithms for least squares
646 support vector machine and kernel ridge regression. *Pattern Recognit.*, 40 (8),
647 2154-2162.
- 648 Ashouri, H., Hsu, K.-L., Sorooshian, S., Braithwaite, D.K., Knapp, K.R., Cecil, L.D.,
649 Nelson, B.R., Prat, O.P., 2015. PERSIANN-CDR: Daily Precipitation Climate
650 Data Record from Multisatellite Observations for Hydrological and Climate
651 Studies. *Bulletin of the American Meteorological Society*, 96 (1), 69-83.
- 652 Baez-Villanueva, O.M., Zambrano-Bigiarini, M., Beck, H.E., McNamara, I., Ribbe,
653 L., Nauditt, A., Birkel, C., Verbist, K., Giraldo-Osorio, J.D., Xuan Thinh, N., 2020.
654 RF-MEP: A novel Random Forest method for merging gridded precipitation
655 products and ground-based measurements. *Remote Sensing of Environment*, 239,



- 656 111606.
- 657 Bai, X., Wu, X., Wang, P., 2019. Blending long-term satellite-based precipitation data
658 with gauge observations for drought monitoring: Considering effects of different
659 gauge densities. *Journal of Hydrology*, 577, 124007.
- 660 Beck, H.E., van Dijk, A.I.J.M., Levizzani, V., Schellekens, J., Miralles, D.G., Martens,
661 B., de Roo, A., 2017. MSWEP: 3-hourly 0.25° global gridded precipitation (1979–
662 2015) by merging gauge, satellite, and reanalysis data. *Hydrology and Earth
663 System Sciences*, 21 (1), 589-615.
- 664 Beck, H.E., Wood, E.F., Pan, M., Fisher, C.K., Miralles, D.G., van Dijk, A.I.J.M.,
665 McVicar, T.R., Adler, R.F., 2019. MSWEP V2 Global 3-Hourly 0.1° Precipitation:
666 Methodology and Quantitative Assessment. *Bulletin of the American
667 Meteorological Society*, 100 (3), 473-500.
- 668 Belgiu, M., Drăguț, L.J.I.J.o.P., Sensing, R., 2016. Random forest in remote sensing:
669 A review of applications and future directions. 114, 24-31.
- 670 Berndt, C., Haberlandt, U., 2018. Spatial interpolation of climate variables in
671 Northern Germany-Influence of temporal resolution and network density. *Journal
672 of Hydrology-Regional Studies*, 15, 184-202.
- 673 Berndt, C., Rabiei, E., Haberlandt, U., 2014. Geostatistical merging of rain gauge and
674 radar data for high temporal resolutions and various station density scenarios.
675 *Journal of Hydrology*, 508, 88-101.
- 676 Bhuiyan, M.A.E., Nikolopoulos, E.I., Anagnostou, E.N., Quintana-Seguí, P.,
677 Barella-Ortiz, A., 2018. A nonparametric statistical technique for combining global
678 precipitation datasets: development and hydrological evaluation over the Iberian
679 Peninsula. *Hydrology and Earth System Sciences*, 22 (2), 1371-1389.
- 680 Bhuiyan, M.A.E., Yang, F., Biswas, N.K., Rahat, S.H., Neelam, T.J., 2020. Machine
681 Learning-Based Error Modeling to Improve GPM IMERG Precipitation Product
682 over the Brahmaputra River Basin. *Forecasting*, 2 (3), 248-266.
- 683 Breiman, L., 2001. Random Forests. *Machine Learning*, 45 (1), 5-32.
- 684 Brocca, L., Filippucci, P., Hahn, S., Ciabatta, L., Massari, C., Camici, S., Schüller, L.,



- 685 Bojkov, B., Wagner, W., 2019. SM2RAIN–ASCAT (2007–2018): global daily
686 satellite rainfall data from ASCAT soil moisture observations. *Earth System*
687 *Science Data*, 11 (4), 1583-1601.
- 688 Brunsell, N.A., 2006. Characterization of land-surface precipitation feedback regimes
689 with remote sensing. *Remote Sensing of Environment*, 100 (2), 200-211.
- 690 Chao, L., Zhang, K., Li, Z., Zhu, Y., Wang, J., Yu, Z., 2018. Geographically weighted
691 regression based methods for merging satellite and gauge precipitation. *Journal of*
692 *Hydrology*, 558, 275-289.
- 693 Cheema, M.J.M., Bastiaanssen, W.G.M., 2012. Local calibration of remotely sensed
694 rainfall from the TRMM satellite for different periods and spatial scales in the
695 Indus Basin. *International Journal of Remote Sensing*, 33 (8), 2603-2627.
- 696 Chen, C., Li, Y., 2019. A fast global interpolation method for digital terrain model
697 generation from large LiDAR-derived data. *Remote Sensing*, 11 (11), 1324.
- 698 Chen, C., Yang, S., Li, Y., 2020a. Accuracy Assessment and Correction of SRTM
699 DEM using ICESat/GLAS Data under Data Coregistration. *Remote Sensing*, 12
700 (20), 3435.
- 701 Chen, C., Zhao, S., Duan, Z., Qin, Z., 2015. An Improved Spatial Downscaling
702 Procedure for TRMM 3B43 Precipitation Product Using Geographically Weighted
703 Regression. *IEEE Journal of Selected Topics in Applied Earth Observations and*
704 *Remote Sensing*, 8 (9), 4592-4604.
- 705 Chen, F., Gao, Y., Wang, Y., Li, X., 2020b. A downscaling-merging method for
706 high-resolution daily precipitation estimation. *Journal of Hydrology*, 581, 124414.
- 707 Chen, F., Liu, Y., Liu, Q., Li, X., 2014. Spatial downscaling of TRMM 3B43
708 precipitation considering spatial heterogeneity. *International Journal of Remote*
709 *Sensing*, 35 (9), 3074-3093.
- 710 Chen, J., Brissette, F.P., Chaumont, D., Braun, M., 2013. Finding appropriate bias
711 correction methods in downscaling precipitation for hydrologic impact studies
712 over North America. *Water Resources Research*, 49 (7), 4187-4205.
- 713 Chen, S.-T., Yu, P.-S., Tang, Y.-H., 2010. Statistical downscaling of daily precipitation



- 714 using support vector machines and multivariate analysis. *Journal of Hydrology*,
715 385 (1), 13-22.
- 716 Chen, S., Xiong, L., Ma, Q., Kim, J.-S., Chen, J., Xu, C.-Y., 2020c. Improving daily
717 spatial precipitation estimates by merging gauge observation with multiple
718 satellite-based precipitation products based on the geographically weighted ridge
719 regression method. *Journal of Hydrology*, 589, 125156.
- 720 Chen, Y., Huang, J., Sheng, S., Mansaray, L.R., Liu, Z., Wu, H., Wang, X., 2018. A
721 new downscaling-integration framework for high-resolution monthly precipitation
722 estimates: Combining rain gauge observations, satellite-derived precipitation data
723 and geographical ancillary data. *Remote Sensing of Environment*, 214, 154-172.
- 724 Duan, Z., Bastiaanssen, W.G.M., 2013. First results from Version 7 TRMM 3B43
725 precipitation product in combination with a new downscaling-calibration
726 procedure. *Remote Sensing of Environment*, 131, 1-13.
- 727 Elnashar, A., Zeng, H., Wu, B., Zhang, N., Tian, F., Zhang, M., Zhu, W., Yan, N.,
728 Chen, Z., Sun, Z., Wu, X., Li, Y., 2020. Downscaling TRMM Monthly
729 Precipitation Using Google Earth Engine and Google Cloud Computing. *Remote
730 Sensing*, 12 (23).
- 731 Fan, D., Wu, H., Dong, G., Jiang, X., Xue, H., 2019. A Temporal Disaggregation
732 Approach for TRMM Monthly Precipitation Products Using AMSR2 Soil
733 Moisture Data. *Remote Sensing*, 11 (24).
- 734 Funk, C., Peterson, P., Landsfeld, M., Pedreros, D., Verdin, J., Shukla, S., Husak, G.,
735 Rowland, J., Harrison, L., Hoell, A., Michaelsen, J., 2015. The climate hazards
736 infrared precipitation with stations—a new environmental record for monitoring
737 extremes. *Scientific Data*, 2 (1), 150066.
- 738 Gebregiorgis, A.S., Hossain, F., 2013. Understanding the Dependence of Satellite
739 Rainfall Uncertainty on Topography and Climate for Hydrologic Model
740 Simulation. *IEEE Transactions on Geoscience and Remote Sensing*, 51 (1),
741 704-718.
- 742 Georganos, S., Grippa, T., Niang Gadiaga, A., Linard, C., Lennert, M., Vanhuyse, S.,



- 743 Mboga, N., Wolff, E., Kalogirou, S., 2019. Geographical random forests: a spatial
744 extension of the random forest algorithm to address spatial heterogeneity in
745 remote sensing and population modelling. *Geocarto International*, 1-16.
- 746 Goovaerts, P., 2000. Geostatistical approaches for incorporating elevation into the
747 spatial interpolation of rainfall. *J. Hydrol.*, 228 (1-2), 113-129.
- 748 Haile, A.T., Habib, E., Rientjes, T., 2013. Evaluation of the climate prediction center
749 (CPC) morphing technique (CMORPH) rainfall product on hourly time scales
750 over the source of the Blue Nile River. *Hydrological Processes*, 27 (12),
751 1829-1839.
- 752 Hengl, T., Nussbaum, M., Wright, M.N., Heuvelink, G.B., Gräler, B.J.P., 2018.
753 Random forest as a generic framework for predictive modeling of spatial and
754 spatio-temporal variables. *PeerJ*, 6, e5518.
- 755 Hou, A.Y., Kakar, R.K., Neeck, S., Azarbarzin, A.A., Kummerow, C.D., Kojima, M.,
756 Oki, R., Nakamura, K., Iguchi, T., 2014. The Global Precipitation Measurement
757 Mission. *Bulletin of the American Meteorological Society*, 95 (5), 701-722.
- 758 Huffman, G., Bolvin, D., Braithwaite, D., Hsu, K., Joyce, R., 2019. Algorithm
759 theoretical basis document (ATBD) NASA global precipitation measurement
760 (GPM) integrated multi-satellite Retrievals for GPM (IMERG). Nasa (December),
761 29.
- 762 Huffman, G.J., Bolvin, D.T., Nelkin, E.J., Wolff, D.B., Adler, R.F., Gu, G., Hong, Y.,
763 Bowman, K.P., Stocker, E.F., 2007. The TRMM Multisatellite Precipitation
764 Analysis (TMPA): Quasi-Global, Multiyear, Combined-Sensor Precipitation
765 Estimates at Fine Scales. *Journal of Hydrometeorology*, 8 (1), 38-55.
- 766 Immerzeel, W.W., Rutten, M.M., Droogers, P., 2009. Spatial downscaling of TRMM
767 precipitation using vegetative response on the Iberian Peninsula. *Remote Sensing
768 of Environment*, 113 (2), 362-370.
- 769 Jia, S., Zhu, W., Lü, A., Yan, T., 2011. A statistical spatial downscaling algorithm of
770 TRMM precipitation based on NDVI and DEM in the Qaidam Basin of China.
771 *remote sensing of environment*, 115 (12), 3069-3079.



- 772 Jing, W., Yang, Y., Yue, X., Zhao, X., 2016. A Spatial Downscaling Algorithm for
773 Satellite-Based Precipitation over the Tibetan Plateau Based on NDVI, DEM, and
774 Land Surface Temperature. *Remote Sensing*, 8 (8).
- 775 Karbalaye Ghorbanpour, A., Hessels, T., Moghim, S., Afshar, A., 2021. Comparison
776 and assessment of spatial downscaling methods for enhancing the accuracy of
777 satellite-based precipitation over Lake Urmia Basin. *Journal of Hydrology*, 596,
778 126055.
- 779 Li, M., Shao, Q., 2010. An improved statistical approach to merge satellite rainfall
780 estimates and raingauge data. *Journal of Hydrology*, 385 (1), 51-64.
- 781 Li, T., Shen, H., Yuan, Q., Zhang, X., Zhang, L., 2017. Estimating ground - level
782 PM2.5 by fusing satellite and station observations: a geo-intelligent deep learning
783 approach. *Geophysical Research Letters*, 44 (23), 11,985-911,993.
- 784 Li, Y., Zhang, Y., He, D., Luo, X., Ji, X., 2019. Spatial Downscaling of the Tropical
785 Rainfall Measuring Mission Precipitation Using Geographically Weighted
786 Regression Kriging over the Lancang River Basin, China. *Chinese Geographical
787 Science*, 29 (3), 446-462.
- 788 Lin, A., Wang, X.L., 2011. An algorithm for blending multiple satellite precipitation
789 estimates with in situ precipitation measurements in Canada. *Journal of
790 Geophysical Research: Atmospheres*, 116 (D21).
- 791 Lu, X., Tang, G., Wang, X., Liu, Y., Jia, L., Xie, G., Li, S., Zhang, Y., 2019.
792 Correcting GPM IMERG precipitation data over the Tianshan Mountains in China.
793 *Journal of Hydrology*, 575, 1239-1252.
- 794 Lu, X., Tang, G., Wang, X., Liu, Y., Wei, M., Zhang, Y., 2020. The Development of a
795 Two-Step Merging and Downscaling Method for Satellite Precipitation Products.
796 *Remote Sensing*, 12 (3).
- 797 Ma, Z., Shi, Z., Zhou, Y., Xu, J., Yu, W., Yang, Y., 2017. A spatial data mining
798 algorithm for downscaling TMPA 3B43 V7 data over the Qinghai–Tibet Plateau
799 with the effects of systematic anomalies removed. *Remote Sensing of
800 Environment*, 200, 378-395.



- 801 Mohsenzadeh Karimi, S., Kisi, O., Porrajabali, M., Rouhani-Nia, F., Shiri, J., 2020.
802 Evaluation of the support vector machine, random forest and geo-statistical
803 methodologies for predicting long-term air temperature. *ISH Journal of Hydraulic*
804 *Engineering*, 26 (4), 376-386.
- 805 Park, N.-W., Kyriakidis, P.C., Hong, S., 2017. Geostatistical Integration of Coarse
806 Resolution Satellite Precipitation Products and Rain Gauge Data to Map
807 Precipitation at Fine Spatial Resolutions. *Remote Sensing*, 9 (3), 255.
- 808 Pham, B.T., Le, L.M., Le, T.-T., Bui, K.-T.T., Le, V.M., Ly, H.-B., Prakash, I., 2020.
809 Development of advanced artificial intelligence models for daily rainfall
810 prediction. *Atmospheric Research*, 237, 104845.
- 811 R. Lima, C.H., Kwon, H.-H., Kim, Y.-T., 2021. A Bayesian Kriging Model Applied
812 for Spatial Downscaling of Daily Rainfall from GCMs. *Journal of Hydrology*,
813 126095.
- 814 Sachindra, D.A., Ahmed, K., Rashid, M.M., Shahid, S., Perera, B.J.C., 2018.
815 Statistical downscaling of precipitation using machine learning techniques.
816 *Atmospheric Research*, 212, 240-258.
- 817 Sharifi, E., Saghafian, B., Steinacker, R., 2019. Downscaling Satellite Precipitation
818 Estimates With Multiple Linear Regression, Artificial Neural Networks, and
819 Spline Interpolation Techniques. *Journal of Geophysical Research Atmospheres*,
820 124 (2), 789-805.
- 821 Shi, Y., Song, L., Xia, Z., Lin, Y., Myneni, R.B., Choi, S., Wang, L., Ni, X., Lao, C.,
822 Yang, F., 2015. Mapping Annual Precipitation across Mainland China in the
823 Period 2001–2010 from TRMM3B43 Product Using Spatial Downscaling
824 Approach. *Remote Sensing*, 7 (5), 5849-5878.
- 825 Sun, L., Lan, Y., 2021. Statistical downscaling of daily temperature and precipitation
826 over China using deep learning neural models: Localization and comparison with
827 other methods. *International Journal of Climatology*, 41 (2), 1128-1147.
- 828 Tao, Y., Gao, X., Hsu, K., Sorooshian, S., Ihler, A., 2016. A Deep Neural Network
829 Modeling Framework to Reduce Bias in Satellite Precipitation Products. *Journal*



- 830 of Hydrometeorology, 17 (3), 931-945.
- 831 Ullah, S., Zuo, Z., Zhang, F., Zheng, J., Huang, S., Lin, Y., Iqbal, I., Sun, Y., Yang, M.,
832 Yan, L., 2020. GPM-Based Multitemporal Weighted Precipitation Analysis Using
833 GPM_IMERGDF Product and ASTER DEM in EDBF Algorithm. Remote
834 Sensing, 12 (19).
- 835 Wang, L., Chen, R., Han, C., Yang, Y., Liu, J., Liu, Z., Wang, X., Liu, G., Guo, S.,
836 2019. An Improved Spatial–Temporal Downscaling Method for TRMM
837 Precipitation Datasets in Alpine Regions: A Case Study in Northwestern China’s
838 Qilian Mountains. Remote Sensing, 11 (7).
- 839 Wang, X., Lin, A., 2015. An algorithm for integrating satellite precipitation estimates
840 with in situ precipitation data on a pentad time scale. Journal of Geophysical
841 Research: Atmospheres, 120 (9), 3728-3744.
- 842 Wu, H., Yang, Q., Liu, J., Wang, G., 2020. A spatiotemporal deep fusion model for
843 merging satellite and gauge precipitation in China. Journal of Hydrology, 584,
844 124664.
- 845 Wu, Z., Zhang, Y., Sun, Z., Lin, Q., He, H., 2018. Improvement of a combination of
846 TMPA (or IMERG) and ground-based precipitation and application to a typical
847 region of the East China Plain. Science of The Total Environment, 640-641,
848 1165-1175.
- 849 Xie, P., Xiong, A.-Y., 2011. A conceptual model for constructing high-resolution
850 gauge-satellite merged precipitation analyses. Journal of Geophysical Research:
851 Atmospheres, 116 (D21).
- 852 Xu, S., Wu, C., Wang, L., Gonsamo, A., Shen, Y., Niu, Z., 2015. A new satellite-based
853 monthly precipitation downscaling algorithm with non-stationary relationship
854 between precipitation and land surface characteristics. Remote Sensing of
855 Environment, 162, 119-140.
- 856 Yan, X., Chen, H., Tian, B., Sheng, S., Wang, J., Kim, J.-S., 2021. A Downscaling–
857 Merging Scheme for Improving Daily Spatial Precipitation Estimates Based on
858 Random Forest and Cokriging. Remote Sensing, 13 (11), 2040.



- 859 Yang, Y., Luo, Y., 2014. Using the Back Propagation Neural Network Approach to
860 Bias Correct TMPA Data in the Arid Region of Northwest China. *Journal of*
861 *Hydrometeorology*, 15 (1), 459-473.
- 862 Yang, Z., Hsu, K., Sorooshian, S., Xu, X., Braithwaite, D., Zhang, Y., Verbist, K.M.J.,
863 2017. Merging high - resolution satellite - based precipitation fields and point -
864 scale rain gauge measurements—A case study in Chile. *Journal of Geophysical*
865 *Research: Atmospheres*, 122 (10), 5267-5284.
- 866 Zambrano-Bigiarini, M., Nauditt, A., Birkel, C., Verbist, K., Ribbe, L., 2017.
867 Temporal and spatial evaluation of satellite-based rainfall estimates across the
868 complex topographical and climatic gradients of Chile. *Hydrol. Earth Syst. Sci.*,
869 21 (2), 1295-1320.
- 870 Zhang, L., Li, X., Zheng, D., Zhang, K., Ma, Q., Zhao, Y., Ge, Y., 2021. Merging
871 multiple satellite-based precipitation products and gauge observations using a
872 novel double machine learning approach. *Journal of Hydrology*, 594.
- 873 Zhang, X., Tang, Q., 2015. Combining satellite precipitation and long-term ground
874 observations for hydrological monitoring in China. *Journal of Geophysical*
875 *Research: Atmospheres*, 120 (13), 6426-6443.
- 876 Zhao, T., Yatagai, A., 2014. Evaluation of TRMM 3B42 product using a new
877 gauge-based analysis of daily precipitation over China. *International Journal of*
878 *Climatology*, 34 (8), 2749-2762.
- 879